ACS APPLIED MATERIALS & INTERFACES

www.acsami.org

Research Article

Controlling the Morphology and Interface of the Perovskite Layer for Scalable High-Efficiency Solar Cells Fabricated Using Green Solvents and Blade Coating in an Ambient Environment

Shih-Han Huang, Kuo-Yu Tian, Hung-Che Huang, Chia-Feng Li, Wei-Cheng Chu, Kun-Mu Lee, Yu-Ching Huang,* and Wei-Fang Su*

Cite This: *ACS Appl. Mater. Interfaces* 2020, 12, 26041−26049

Read Online

ACCESS | Metrics & More | Article Recommendations | Supporting Information

ABSTRACT: Low-cost and solution-processed perovskite solar cells have shown great potential for scaling-up mass production. In comparison with the spin coating process for fabricating devices with small areas, the blade coating process is a facile technique for preparing uniform films with large areas. High-efficiency perovskite solar cells have been reported using blade coating, but they were fabricated using the toxic solvent *N*,*N*-dimethylformide (DMF) in nitrogen. In this work, we present highly efficient blade-coated perovskite solar cells prepared using a green solvent mixture of γ-butyrolactone (GBL) and dimethyl sulfoxide (DMSO) in an ambient environment. By carefully controlling the interface, morphology, and crystallinity of perovskite films through composition variations and additives, a high power conversion efficiency of 17.02% is achieved in air with 42.4% reduction of standard deviation in performance. The findings in this work resolve the issues of scalability and solvent toxicity; thus, the mass production of perovskite solar cells becomes feasible.

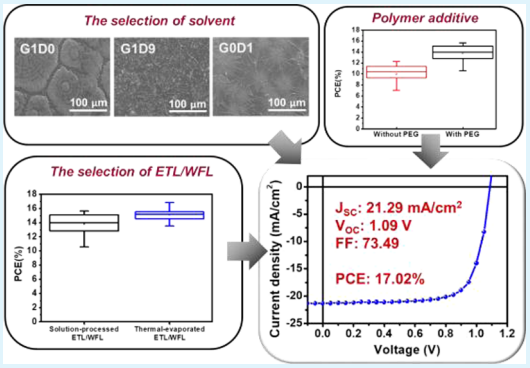

KEYWORDS: *perovskite solar cell, blade coating, morphology, interface, large-area, ambient, green solvent*

INTRODUCTION

Compared to the conventional silicon and copper indium gallium selenide (CIGS) solar cells, organic−inorganic perovskite solar cells (PSCs) exhibit a competitive edge in the market due to their certified power conversion efficiency (PCE) of 25.2% and solution processability. The perovskite has a high absorption coefficient, long carrier diffusion length, low exciton dissociation energy, and good charge carrier mobility, which result in high device performance.[1−5] The spin coating process is not scalable for commercialization, although it can obtain highly efficient PSCs. The structure of planar PSCs can be divided into normal (n-i-p) and inverted (p-i-n) structures, depending on the transportation direction of electrons and holes. The commonly used configuration of n-i-p-type PSCs is fluorine-doped tin oxide (FTO)/c-TiO_2/meso-TiO_2/perovskite/Spiro-OMeTAD/Ag,[6,7] and that of p-i-n-type PSCs is FTO/NiO_x/perovskite/[6,6]-phenyl-C_{61}-butyric acid methyl ester (PCBM)/polyethyleneimine (PEI)/Ag.[8,9] Recently, many techniques have been developed to manufacture large-area PSCs, including inkjet printing,[10,11] spray coating,[12−15] electrodeposition,[16−18] slot-die coating,[19−23] and blade coating.[24−30] Blade coating is different from spin coating in the drying mechanism and can be transferred to a roll-to-roll continuous mass production process. Huang et al. reported a PCE of 15.1% of p-i-n planar PSCs using a doctor-bladed perovskite layer.[24] However, the device was fabricated using the toxic solvent *N*,*N*-dimethylformamide (DMF) in a N_2 atmosphere. The two limiting factors for the mass production of PSCs are the use of a toxic solvent and the need to process in a N_2 atmosphere. Guerrero et al. showed that blade-coated n-i-p PSCs achieved the PCEs of 18.0 and 15.6% when the devices were fabricated with a nontoxic solvent in a dry box and in ambient conditions, respectively.[29] They demonstrated that the blade coating process can cause spherulitic growth in a supersaturating regime and promote the growth of highly crystalline perovskites. However, there is still a PCE gap between the blade-coated PSCs fabricated in an ambient environment (RH ∼ 45 ± 10%) and the spin-coated PSCs fabricated in dry air (RH < 0.01%). In addition, n-i-p structure PSCs usually use a high-temperature-processed TiO_2 layer as an electron transport layer (ETL) and exhibit a hysteresis issue in the device.[31,32] This high-temperature-processed layer increases the cost of manufacturing and limits the chances of

Received: April 4, 2020
Accepted: May 21, 2020
Published: May 21, 2020

https://dx.doi.org/10.1021/acsami.0c06211
ACS Appl. Mater. Interfaces 2020, 12, 26041−26049

flexible PSC manufacturing. Although many low-temperature-processed ETLs are also efficient in transporting electrons and blocking holes in the n-i-p structure PSCs,[33,34] the commonly used hole transport layer (HTL), spiro-OMeTAD, requires doped salts to have good hole transport mobility.[35,36] However, doping salts are considered to be the main reason for the poor operating lifetime of PSCs.[37,38] The PSCs with the p-i-n structure is derived from the organic solar cells, exhibiting the great potential for low-temperature fabrication on flexible substrates and no hysteresis issue in the device. In addition, the used ETL and HTL in the p-i-n structure PSCs usually exhibit sufficient charge mobility without salt doping, which implies that PSCs with a p-i-n structure exhibits improved operating stability as compared with n-i-p structure PVSCs.

Many studies have reported that the morphology and nanostructure of the perovskite film are critical to the PCE of PSCs. The perovskite film quality is strongly dependent on the coating atmosphere, precursor formulation, and additional treatment (antisolvent). However, these studies mainly focus on the devices fabricated by the spin coating process in a N_2 environment. In our previous study, we have noticed that the film formation mechanisms are different between spin coating and large-area coating processes such as slot-die coating.[39] Unlike the spin coating process, we can manipulate the early-stage film crystallization during the transformation of a wet film into a solid-state film by additional heat treatment in the large-area coating process. We have proven that manipulation has a considerable impact on the performance of thin-film solar cells. Furthermore, we use near-infrared irradiation to rapidly fabricate PSCs using the large-area coating process in an ambient environment.[23] Our previous results have demonstrated that the control of film crystallinity and morphology at the early stage is essential to the quality of large-area films. However, a detailed understanding of how to control the formation of the blade-coated perovskite film in ambient conditions is still lacking.

In this study, we systematically investigate the effect of perovskite precursor composition variations on the performance of blade-coated p-i-n PSCs using nontoxic solvents in an ambient environment. First, we applied theories of the Hansen solubility parameter (HSP)[40] and donor number (DN) of the solute and the solvent[41,42] to explore the relationship between a relatively less harmful solvent and a perovskite precursor. A blend of γ-butyrolactone (GBL) and dimethyl sulfoxide (DMSO) was determined as the host solvent of the perovskite precursor. We optimize the PCE of blade-coated PSCs by varying the blend ratio of GBL and DMSO. In addition, we clarify how the compositions of the solvent blend affect the morphology and crystallization of the blade-coated perovskite film. Our results reveal that the nanostructure of blade-coated perovskite films and the power conversion efficiency of devices are influenced greatly by the solvent composition. Moreover, the devices exhibited a larger standard deviation of PCE when they were fabricated by the blade coating process than those by the spin coating process. We speculate that the large PCE standard deviation mainly results from the nonuniformity of the perovskite film and poor interfacial contact between the perovskite film and the top electrode. By adding poly(ethylene glycol) (PEG) into the perovskite precursor solution, a uniform perovskite film can be obtained with a 34.3% reduction of the standard deviation of PCE. The standard deviation is reduced further to 42.4% by improving the interfaces among the electron transport layer, work function layer, and electrode using thermally evaporated C60/bathocuproine (BCP) instead of solution-processed PCBM/PEI. Thus, the current record-high PCE of 17.02% is achieved for blade-coated p-i-n PSCs using relatively less harmful solvents in ambient conditions. This study provides insights into the fabrication of high-efficiency PSCs via the scalable blade coating process.

EXPERIMENTAL SECTION

Preparation of the Solution. In ambient conditions (25−30 °C, 40−60% RH), 0.5 M acetate tetrahydrate ($Ni(CH_3COO)_2{\cdot}4H_2O$, 99.0%, SHOWA Chemical) was dissolved in ethanol (anhydrous, Fisher Chemical) to prepare a NiO_x precursor solution. The solution was then stirred at 60 °C until it became transparent. After adding 1 M equivalent of ethanolamine (99%, Acros Organics), the solution was filtered with 0.22 μm poly(1,1,2,2-tetrafluoroethylene) (PTFE). The following three solutions were prepared in a N_2 glovebox for 4 h before using them. The perovskite precursor solution 0.6 M $CH_3NH_3PbI_3$ was prepared by mixing CH_3NH_3I (MAI, STAREK Scientific Co. Ltd.) and lead iodide (PbI_2, 99.9985%, Alfa Aesar) with a stoichiometric ratio of different solvents such as dimethylformamide (DMF, anhydrous, Acros Organics), γ-butyrolactone (GBL, >99%, Acros Organics), and dimethyl sulfoxide (DMSO, >99.7%, Acros Organics) or GBL/DMSO mixture. For the perovskite precursor of the polymer additive system, the solution contained 0.05 wt % PEG (average M_w, 6k; Acros Organics). [6,6]-Phenyl-C_{61}-butyric acid methyl ester (PCBM, 99.5%, Solenne B.V.) was dissolved in chlorobenzene (20 mg/mL). The work function modifier contained 0.1 wt % polyethyleneimine (PEI, linear, Average M_n 10k, Sigma-Aldrich) in isopropanol (IPA, 99.5%, Acros Organics).

Device Fabrication. The 4 cm × 4 cm FTO-coated glass substrates (Hartford, TEC7) were cleaned by sequential sonication in detergent, hydrogen peroxide/ammonia aqueous solutions, methanol, and isopropanol. The substrates were treated with UV-Ozone for 15 min. The p-type layer NiO_x was spin-coated on the FTO at 4000 rpm for 20 s and annealed for 30 min at 300 °C. Then, 200 μL of the perovskite precursor solution was blade-coated on a 150 °C heated NiO_x-coated substrate at a rate of 1 m/min in an ambient environment. The gap between the blade and substrate was in the range of 190−200 μm. For the solution-processed ETL, the following coating processes were performed in a N_2 glovebox: 150 μL of PCBM solution and 300 μL of PEI solution were deposited by spin coating at 1000 rpm for 30 s and at 3000 rpm for 30 s in sequence. For the thermal-evaporated ETL, 30 nm of C_{60} and 5 nm of BCP were thermally evaporated in sequence. Finally, 100 nm of silver (Ag) electrodes was vacuum deposited on the coated substrate at 5.0 × 10^{-6} mbar to make devices with an active area of 0.09 cm^2.

Characterization of Perovskite Films and Devices. Scanning electron microscopy (SEM) (S3000N, Hitachi) and atomic force microscopy (AFM) (Dimension-3100 Multimode, Digital Instruments) were used for the morphology studies. The crystal structures of perovskite films were characterized using an X-ray diffractometer (XRD, TTRAX iii, Rigaku). Grazing-incident wide-angle X-ray scattering (GIWAXS) measurements were performed using a monochromatic X-ray beam with a wavelength of 1.33 Å and an incidence angle of 0.2° at the 17A beamline of the National Synchrotron Radiation Research Center (NSRRC), Taiwan. The photoluminescence (PL) spectra and time-resolved PL (TRPL) were performed by exciting perovskite with a 532 nm diode laser (LDH-P-C-405, PicoQuant). The TRPL was recorded by a system (UniDRON-plus, UniNano Tech). Electrochemical impedance spectroscopy (EIS) was measured by an impedance measurement unit (elektrik PP210, ZAHNER) under illumination. The frequency ranging from 10 kHz to 100 MHz was used. The $I-V$ characteristics of the device were measured using a voltage source meter (Keithley 2410) under an AM 1.5 solar simulator (YSS-150A, YAMASHITA DENSO) with an irradiation intensity of 100 mW/cm^2. The statistical distribution of the photovoltaic parameters was calculated using at least 20 devices.

https://dx.doi.org/10.1021/acsami.0c06211
ACS Appl. Mater. Interfaces 2020, 12, 26041−26049

Table 1. Summary of the Calculated Hansen Solubility Parameters and Donor Numbers for Different Solvents

solvent[a]	toxic	δD	δP	δH	Hansen distance (R_a)	donor number (kcal/mol)	dissolution	bp (°C)
DMF	yes	17.4	13.7	11.3	0	26.6	yes	153
DMAC	yes	17.0	11.6	10.2	2.60	27.8	yes	165
NMP	yes	18.0	12.3	7.2	4.50	27.3	yes	202
acetonitrile	yes	15.3	18.0	6.1	7.95	14.1	no	82
TEA	no	15.5	0.4	1.0	17.45	61.0	yes	89
DMSO	no	18.4	16.4	10.2	3.54	29.8	yes	189
GBL	no	18.0	16.6	7.4	5.01	18.0	yes	204
DEF	no	16.4	10.9	6.0	6.20	30.9	no	176
1-butanol	no	16.0	5.7	15.8	9.60	29.0	no	118

[a]*N*,*N*-Dimethylformamide (DMF), *N*,*N*-dimethylacetamide (DMAC), *N*-methyl-2-pyrrolidone (NMP), triethylamine (TEA), dimethyl sulfoxide (DMSO), γ-butyrolactone (GBL), and *N*,*N*-diethylformamide (DEF).

RESULTS AND DISCUSSION

The perovskite precursor solvent of DMF is widely used for obtaining high-efficiency blade-coated PSCs;[24−28,30] however, the DMF solvent is carcinogenic to humans. Therefore, alternative solvents to DMF are necessary to ensure a safe mass production process. In addition, the raw materials of the perovskite film, i.e., methylamine iodide (MAI) and lead iodide (PbI_2), should be easily dissolved in the perovskite precursor solvent.[43−45] We use the semiexperimental theory of the Hansen solubility parameter to predict the dissolution relationship between the solute and solvent, which is expressed as the Hansen distance (R_a).[40] The R_a is calculated as the follows

$$(R_a)^2 = 4(\delta D_2 - \delta D_1)^2 + (\delta P_2 - \delta P_1)^2 + (\delta H_2 - \delta H_1)^2 \quad (1)$$

where δD is the van der Waals force, δP is the intermolecular dipole moment, and δH is the hydrogen bond. Thus, R_a is calculated based on the change in δH, δP, and δD between two different solvents. We set the R_a of a commonly used solvent, DMF, at zero. The smaller the value of R_a of a given solvent, the better the solubility of the perovskite precursor materials in this solvent. However, perovskite materials are hybrid materials consisting of organic and ionic materials. The interactions between the ionic material and the solvent, such as solvation and adducts formation, are not considered in the HSP model.[45] The HSP model cannot be applied well to the selection of a suitable solvent for perovskite solar cells due to the ionic content. Thus, we used the donor number (DN) in addition to quantify the possibility of adduct formation and represent the ease and the energy of adduct formation.[41,42] We can select the proper solvents for the perovskite precursor by considering both HSP and DN simultaneously.

Table 1 lists the calculated R_a and DN of the commonly used solvents, including toxic solvents and relatively less harmful solvents, in the perovskite precursor. Figure 1a shows a plot of DN versus Hansen distance for various solvents. The solvents represented by the open symbols and solid symbols indicate whether they can dissolve the perovskite precursor or not, respectively. These solvents can be divided into three regions; the solvents located in region 1 exhibit a low Hansen distance and they can dissolve perovskite materials well, regardless of their DN values. With increasing Hansen distance, the effect of the DN values on the solubility of perovskite materials became obvious gradually. The solvents located in region 2 show an acceptable solubility for perovskite materials with a DN value larger than 30. The solvents with a high Hansen distance (>6) and low DN (<30), which are located in region 3, reveal a poor solubility for perovskite materials. According to the results of the solubility experiments, we can determine the critical values of the Hansen distance and DN of suitable solvents for perovskite materials. We selected four relatively less harmful solvents, GBL, 1-butanol, DMSO, and triethylamine (TEA) from Figure 1a. The solubility of CH_3NH_3I (MAI) and PbI_2 in these solvents is evaluated.

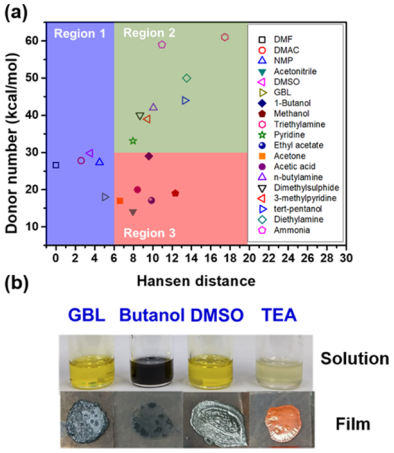

Figure 1. (a) Plot of donor number versus Hansen distance of different solvents related to dimethylformamide (DMF). (b) Photographs of the perovskite precursor solutions and films prepared using different solvents.

Figure 1b shows the four perovskite precursor solutions and their related films. The solutes form a clear solution in the solvents of GBL, DMSO, and TEA. The results indicate that both CH_3NH_3I and PbI_2 have good solubility in these solvents. The high R_a (9.60) of 1-butanol indicates that it is a poor solvent for PbI_2 that results in a nonclear black solution. TEA exhibits very high R_a (17.45) and high DN (61 kcal/mol) as compared to other solvents. The high R_a of TEA exhibits poor solubility toward the perovskite precursor, but the solubility can be increased by its high DN. TEA can form easily with HI that improves the solubility of the precursor in TEA. Then, PbI_2 is easily attracted by the adduct in the solution,[46] and the chemical reactions of dissolution are described below

$$PbI_2 + CH_3NH_3I \xrightarrow[\text{dissolve in } (C_2H_5)_3N]{} (C_2H_5)_3N{\cdot}HI + PbI_2 + CH_3NH_2 \quad (2)$$

https://dx.doi.org/10.1021/acsami.0c06211
ACS Appl. Mater. Interfaces 2020, 12, 26041−26049

$$(C_2H_5)_3N{\cdot}HI + PbI_2 + CH_3NH_2 \xrightarrow{\Delta} (C_2H_5)_3NHPbI_3 \quad (3)$$

We deposited the film using the precursor in TEA and then annealed the film. The annealed film appears red, which indicates that the stable adduct of $(C_2H_5)_3NHPbI_3$ cannot be transformed into perovskites. In summary, the low Hansen distance (less than 6) is critical for the good solubility of MAI and PbI_2 in nontoxic solvents with the DN lower than 30 kcal/mol, as shown by the red dash line in Figure 1a. Therefore, the most suitable less harmful solvents are GBL and DMSO, and they are used in the following study.

We first investigated the effect of solvent type and deposition atmosphere on the surface morphologies of blade-coated perovskite films. Figure 2a,b shows the SEM images of

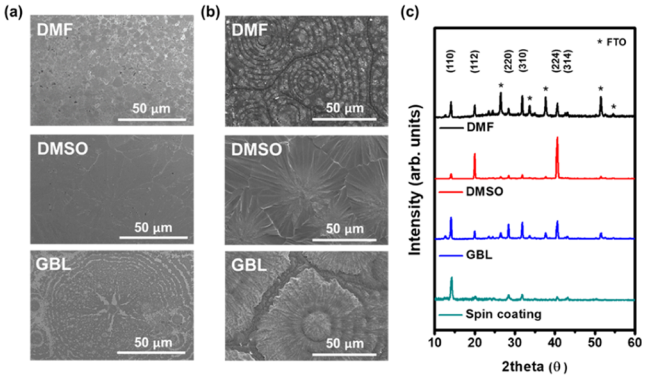

Figure 2. Top-view SEM images of perovskite films prepared using different solvents (a) in nitrogen and (b) in ambient conditions. (c) XRD patterns of perovskite films prepared using different solvents in ambient conditions.

these films. The perovskite films deposited in N_2 show relatively smooth surfaces and small crystallites compared to those deposited in ambient conditions (45−55% RH). The results imply that humidity affects the crystallization behavior of the blade-coated perovskite films. For the films deposited in ambient conditions, the perovskite film based on the DMF-based precursor shows a dense film with concentric circle crystallinities. The film deposited from a DMSO-based precursor shows a wrinkled morphology from the center of the crystal domain, but the film is still dense without excessive pinholes. The film prepared using GBL as the host solvent shows a large domain size and isolated crystal domains. Figure 2c shows the different crystallization behaviors of these perovskite films coated in ambient conditions using X-ray diffraction. The crystal planes of $CH_3NH_3PbI_3$ are (110), (112), (220), (310), (224), and (314), corresponding to angles 14.14, 19.94, 28.50, 31.94, 40.52, and 43.13°, respectively.[47] The X-ray diffraction (XRD) patterns of the perovskite and FTO appear in the film fabricated using a DMF-based precursor in ambient conditions. The results indicate the film is not dense as appeared in the SEM image due to the strong affinity of the amino group of DMF to water in high humidity. The perovskite films fabricated from GBL and DMSO-based precursors do not reveal the FTO phase. Therefore, we studied the effects of solvent type and composition variation of GBL and DMSO on the blade-coated films and the PCE of the PSCs, and the results are summarized and discussed below.

To find the optimum condition, we evaluate the effect of the mixed solvents on the characteristics of photovoltaics directly. Various devices were fabricated and their performances were compared. To obtain the best PCE for blade-coated PSCs, we first adjusted the mixing ratio of GBL to DMSO, which was expected to be the key determining factor of the quality of blade-coated perovskite films. We named the devices by the mixing ratio of the two solvents; for example, for a 9:1 mixing ratio of GBL to DMSO, the devices were named as G9D1. The devices fabricated from the precursors using pristine GBL and DMSO were named as G1D0 and G0D1, respectively.

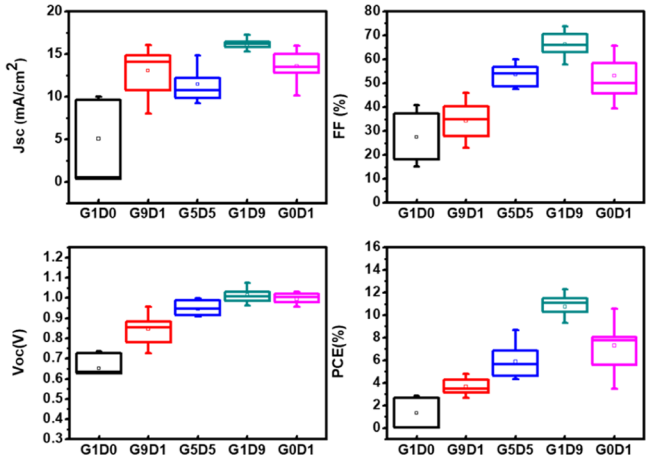

Figure 3. Statistical distribution of PCE, J_{sc}, FF, and V_{oc} of the PSCs fabricated using a solvent mixture of DMSO and GBL at different volume ratios.

Figure 3 and Table 2 summarize the characteristic distribution of blade-coated PSCs obtained from more than ten devices. The related $J-V$ curves are shown in Figure S1 (Supporting Information). Throughout the optimization, the G1D9 devices exhibited an average PCE of 9.55% with the highest PCE of 12.30%. Basically, for different solvent compositions, the trend of PCE is roughly consistent with the trends of open-circuit voltage (V_{oc}), short-circuit current density (J_{sc}), and fill factor (FF); however, the effect on FF is the most significant. The FF is mainly affected by the charge loss behavior such as trap density, charge recombination, and charge transport, which is highly related to the surface morphology and crystallization of the perovskite films.[43] Therefore, we further investigated the surface morphology and crystallinity of these blade-coated perovskite films.

Figure 4 shows the surface morphology and roughness of perovskite films fabricated from different compositions of the solvent mixture using SEM (Figure 4a) and AFM (Figure 4b), respectively. The SEM images captured at high magnification (less than 10 μm) reveal complete perovskite crystals in a small area, which are shown in Figure S2. The root-mean-square (RMS) roughness data are shown in Figure S3 for blade-coated films fabricated from different solvent compositions The morphology of the perovskite film fabricated from pristine GBL is consistent with the SEM image, as shown in Figure 3. There appears to be a large crystal domain and long crack on the film, with an RMS roughness of 82.56 nm. With 10 vol % DMSO added in the GBL, the film becomes dense and shows no cracks, but the roughness is still high. When the blending amount of DMSO increases, the film morphology becomes

https://dx.doi.org/10.1021/acsami.0c06211
ACS Appl. Mater. Interfaces 2020, 12, 26041−26049

Table 2. Performance of PSCs Fabricated Using Different Solvent Mixtures in Ambient Conditions

perovskite solution	J_{sc} (mA/cm^2)	V_{oc} (V)	FF (%)	PCE (%)[a]
G1D0	5.05 ± 5.08	0.65 ± 0.10	27.51 ± 11.44	1.35 ± 1.44 (2.83)
G9D1	13.07 ± 2.49	0.85 ± 0.07	34.31 ± 7.20	3.69 ± 0.67 (4.81)
G5D5	11.46 ± 2.20	0.95 ± 0.03	53.75 ± 4.22	5.89 ± 1.54 (8.70)
G1D9	15.09 ± 2.94	1.03 ± 0.05	60.86 ± 5.53	9.55 ± 2.44 (12.30)
G0D1	13.60 ± 2.10	0.99 ± 0.05	53.14 ± 8.16	7.31 ± 2.03 (10.56)

[a]Champion values are listed in the parentheses.

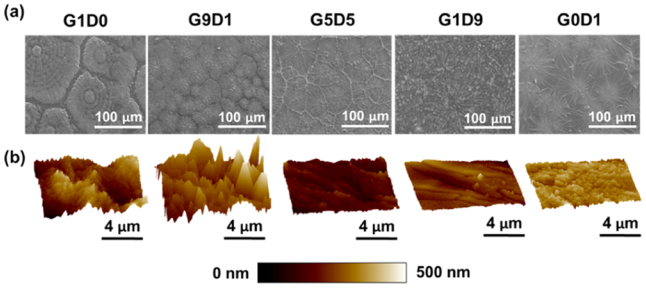

Figure 4. Morphologies of the perovskite films prepared using a solvent mixture of DMSO and GBL at different volume ratios in ambient conditions: (a) top-view SEM images and (b) AFM images.

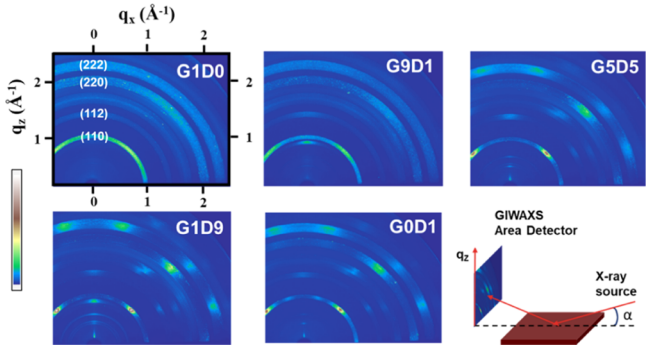

Figure 5. Characteristics of perovskite films prepared using a solvent mixture of DMSO and GBL at different volume ratios in ambient conditions by two-dimensional (2D) GIWAXS patterns.

much smoother and shows no pinholes. In comparison to the film deposited from pristine DMSO, the G1D9 film does not show the flowerlike wrinkles with a clear domain boundary in the film. The film exhibits the lowest roughness of 15.57 nm. According to our previous studies,[23,39] the morphology of the slot-die coated film is greatly influenced by the early stage of film formation from a wet film to a solid film, and the film drying rate is directly related to the boiling point of the perovskite precursor solution. In addition, previous literature works also pointed out that the morphology of blade-coated films is affected by the surface tension of the perovskite precursor solution. They added a suitable surfactant to reduce the surface tension of the perovskite solution and improve the affinity of the perovskite solution with the substrate.[28] Therefore, we also evaluated the surface tension of the perovskite solution using various mixing ratios of the two solvents (GBL and DMSO) by measuring the contact angle of the perovskite solution on a nonwetting substrate. Figure S4 shows the contact angle measurements of the perovskite precursor solution based on pristine DMSO (G0D1) and mixed solvent (10 vol % GBL and 90 vol % DMF, G1D9) on FTO/NiO_x substrates. Reduced surface tension is confirmed by the decreasing contact angle when G1D9 was used as the host solvent for the perovskite precursor. This result implies that the affinity between the perovskite solution and the underlying layer can be improved by tuning the mixing ratio of two solvents, and thus, the morphology of perovskite films strongly depends on the ratio of the mixed solvents.

In addition, we evaluated the crystallization behaviors of perovskite films deposited from different compositions of perovskite precursors using XRD and GIWAXS, as shown in Figures S5 and 5. The XRD patterns (Figure S5) indicate that the orientation of perovskite crystals varies greatly with the precursor solvent composition. As the blending amount of DMSO increases, the preferred orientation switches from the (110) plane to (112) and (224) planes, representing angles of 14.1, 19.8, and 40.5°, respectively. In addition, the two-dimensional (2D) GIWAXS patterns of GBL-dominated films (G1D0 and G9D1) exhibit diffraction rings, which imply the random orientation of the perovskite crystals within the blade-coated films. In contrast, the GIWAXS patterns of the DMSO-rich films (G5D5, G1D9, and G0D1) show pronounced diffraction spots, indicating a high degree of the crystalline order. High donor number (DN) solvents, such as DMSO, interact with perovskite precursors to form an adduct and reduce the surface energy of the lead atom in the perovskite precursor. For a precursor with low surface energy, perovskite crystals prefer to grow along the (110) plane rather than along (112).[48] By increasing the ratio of DMSO in the mixing solvents, the surface energy of the perovskite precursor can be further reduced, leading to the crystallization of perovskite crystals in a preferred orientation along (112). Thus, the smooth surface morphology and high crystallinity of the blade-coated films (G1D9) are contributed to fast charge transport and high power conversion efficiency in PSCs. The results are consistent with the literature.[49] Therefore, one of the key factors for high-efficiency blade-coated PSCs is the composition of the perovskite precursor for achieving a smooth and crystalline perovskite film.

Although we have recognized the effect of the perovskite precursor solvent on the PCE of blade-coated PSCs, it is worth noting that these devices exhibit a relatively large standard deviation in the PCE. For example, the best PCE of the devices based on G1D9 films is 12.3%; however, the average PCE is only 9.55% with a high standard deviation of 2.44%. The issue of large standard deviation in PCE is especially critical in the realization of mass production in the large-area deposition process. We speculate two factors resulting in the large standard deviation in PCE: (i) the uniformity of the blade-coated perovskite film is still lacking and (ii) the interfacial contact is poor between the electron transport layer and blade-coated perovskite film. Previously, we demonstrated that the addition of PEG can effectively tune the film morphology by retarding the growth of perovskite crystals in the spin-coated perovskite films.[50] Therefore, we first added PEG in the perovskite precursor solution to promote the formation of the

https://dx.doi.org/10.1021/acsami.0c06211
ACS Appl. Mater. Interfaces 2020, 12, 26041−26049

continuous uniform blade-coated film. We have used the in situ synchrotron scattering technique to discover the role of PEG in the formation of the perovskite layer from a solution to a solid film fabricated by drop casting.[51] The film formation mechanism in the blade coating process is similar. During the film formation, the PEG additive retards the growth of the intermediate phase. The size of the intermediate crystallites in the perovskite film with PEG is smaller than in the pristine perovskite film. The formation of the perovskite crystallites can be maintained by inhibiting the splitting of the intermediate grains. Therefore, the domain size of the perovskite film with PEG is larger than that of the pristine perovskite film, as shown in the SEM image (Figure S6). The corresponding current density−voltage curves and PCE with standard deviation are shown in Figure 6 and listed in Table 3. In comparison to the

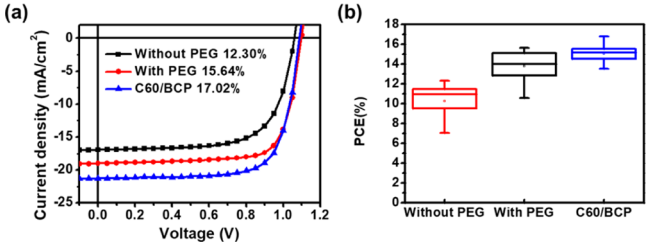

Figure 6. Performance of the perovskite solar cell: (a) $J-V$ curves of the best-performing devices and (b) statistical distribution of PCEs of these devices (without PEG, PEG, and C60/BCP).

devices without PEG, the average PCE of the devices with PEG is more than 13%, and the highest PCE of 15.64% is achieved. In addition to the improvement of average PCE, the standard deviation of PCE is decreased from 2.33 to 1.53% (34.3% improvement). These results imply that the addition of PEG can effectively tune the morphology and improve the uniformity of the blade-coated perovskite films. We further measured the trap density and photoluminescence (PL) spectra of these perovskite films to clarify the role of the PEG additive. The trap density can be calculated by the trap-filled limit (TFL) equation, and the voltage at which all traps are filled is known as the trap-filled-limit voltage (V_{TFL}). For the V_{TFL} measurement, the following device structure is adopted: FTO/NiO_x/perovskite/PTAA/Au. We can obtain the V_{TFL} by fitting the slopes of the space-charge-limited current (SCLC) curve with the following V_{TFL} equation in the trap-filled limit regime, as shown in Figure S7a.

$$V_{TFL} = \frac{eN_t d^2}{2\varepsilon\varepsilon_0} \tag{4}$$

where N_t is the trap density of the film, ε_0 and d represent the vacuum permittivity and the film thickness, respectively, and ε is the average relative dielectric constant of the perovskite film. The thickness of the perovskite layer is around 350 nm, which was measured based on the cross-sectional SEM image (Figure S7b). The calculated V_{TFL} and trap density are listed in Table S1, and the trap density of the perovskite film was reduced from 3.82×10^{16} to 2.76×10^{16} (carriers/cm^3) by adding the PEG additive. The PL spectra shown in Figure S8a indicate that a higher PL intensity for the perovskite film with PEG than that for the pristine perovskite layer, which implies that the perovskite film with PEG exhibits fewer defects and a more homogeneous surface. In addition, time-resolved PL (TRPL) was conducted to demonstrate the charge carrier lifetime of these perovskite layers (Figure S8b). The decays follow a second-order exponential decay trend, which is shown below, and the data are fitted accordingly

$$y(x) = y_0 + A_1 e^{-x/\tau_1} + A_2 e^{-x/\tau_2} \tag{5}$$

A_1 and A_2 are the decay amplitude fractions and τ_1 and τ_2 are the fast and slow decay times, respectively. Moreover, τ_{avg} is introduced to represent the carrier lifetime of the perovskite film and calculated using the following formula

$$\tau_{avg} = \frac{A_1\tau_1 + A_2\tau_2}{A_1 + A_2} \tag{6}$$

All of these parameters are listed in Table S2, and the τ_{avg} values of the pristine perovskite film and the perovskite film with PEG are 25.68 and 48.36 ns, respectively. The long carrier lifetime of the perovskite film implies that the PEG additive passivates the defects inside the perovskite film. In addition to the defects, charge recombination in the perovskite film can also be effectively reduced with the addition of PEG. According to these results, we conclude that the PEG additive can control crystallization and passivate defects, such as grain boundaries within the perovskite films, and thus, larger grain size can be formed.[52] The increase in the grain size of the perovskite film is expected to have long-term stability. We measured the stability of the blade-coated devices by monitoring the changes in PCE with time, as shown in Figure S9. The measurements were done in ambient conditions without encapsulation (25 °C and 50−60 RH%). After 100 h, the PCEs of PSCs prepared using the G0D1 and G1D9 solvents were reduced to 80 and 85% of the initial PCEs, respectively. It indicated that the stability is affected by the various morphologies of the perovskite films resulting from using different solvent compositions. Furthermore, the T_{80} lifetime of PSCs of the two samples without the PEG additive is below 200 h. However, the T_{80} lifetime of PSC with PEG additive is more than 350 h. The results suggest that the improved stability of PSCs with the PEG additive is due to the reduced number of defects in the film. In addition, we demonstrate the performance of a large-area device and module shown in Figure S10. Figure S10a shows the $J-V$ curves of the PSC with a device area of 1 cm^2. The achievable PCE can be up to 12.36%. The blade-coated module (4 cm × 4 cm) is interconnected by five subcells (0.3 cm × 2.5 cm) and exhibits a PCE of 9.81% (Figure S10b), which is compatible

Table 3. Performance of PSCs Fabricated Using Perovskite Films with or without PEG

perovskite solution	J_{sc} (mA/cm^2)	V_{oc} (V)	FF (%)	PCE (%)[a]
without PEG	15.45 ± 2.52	1.03 ± 0.04	62.86 ± 7.59	9.92 ± 2.31 (12.31)
with PEG	18.15 ± 1.18	1.07 ± 0.03	70.93 ± 6.02	13.78 ± 1.53 (15.64)
C60/BCP	20.56 ± 0.77	1.06 ± 0.02	67.70 ± 5.77	14.80 ± 1.33 (17.02)

[a]Champion values are listed in the parentheses.

https://dx.doi.org/10.1021/acsami.0c06211
ACS Appl. Mater. Interfaces 2020, 12, 26041−26049

with that of the large-area device. Furthermore, the interfacial contact between the blade-coated perovskite layer and the adjacent layer is another key factor influencing the standard deviation of PCE. The adjacent layers, including ETL and WFL, are sequentially deposited on the blade-coated perovskite layer. Therefore, the interfacial contact between them is strongly affected by the surface morphology of the under layer. To form a better contact layer on the perovskite layer, we replaced the solvent-processed PCBM and PEI with thermal-evaporated fullerene (C60) and bathocuproine (BCP). The related $J-V$ curve and PCE are presented in Figure 6 and Table 3. These devices show that the standard deviation is further reduced to 1.33% (42.4% cumulative reduction). The average PCE can be further improved to 14.80%, and the highest PCE of 17.02% can be achieved. The enhanced PCEs mainly result from the increasing J_{sc}, which implies that the improvement in the interfacial contact can effectively facilitate the charge transport.[53,54] Electrochemical impedance spectroscopy (EIS) was able to disclose the interfacial charge transport properties between the perovskite film and the upper layer. EIS spectra of PSCs were measured at V_{oc} of each device under illumination conditions, as shown in Figure S11. The equivalent circuit model consisted of a series resistance (R_s), a charge-transfer resistance (R_{CT}) at the interface, and a recombination resistance of the perovskite (R_{rec}). The differences in R_{CT} stem mainly from the interfacial resistance of the PSC with C60/BCP and PCBM/PEI. R_{CT} of PSCs with C60/BCP is smaller than that with PCBM/PEI, revealing more efficient charge transfer in PSC with C60/BCP. Thus, PSCs with C60/BCP exhibit increasing J_{sc} because of the improved interfacial contact. To the best of our knowledge, this is a record-high PCE for the blade-coated PSCs using less harmful solvents in ambient conditions. Our study has successfully verified the impact of surface morphology and interfacial contact on the performance and PCE distribution of the blade-coated PSCs.

CONCLUSIONS

In this study, we used the Hansen distance and donor number to select green solvents DMSO and GBL to fabricate perovskite films using blade coating in ambient conditions. The blending ratio of 9/1 by volume of DMSO and GBL was determined to obtain the best perovskite film with high density and crystallinity. In addition, we successfully fabricated blade-coated PSCs with a high average PCE and a small PCE distribution by adding PEG to modify the surface morphology of the blade-coated films and using thermally evaporated ETL and WFL to exhibit good interfacial contact. The highest PCE of 17.02% can be obtained from the blade-coated PSCs in ambient conditions. Our study provides a simple and feasible method for the manufacturing of less harmful solvents and large-area and air-processed PSCs and paves the way for their future commercialization.

ASSOCIATED CONTENT

Supporting Information

The Supporting Information is available free of charge at https://pubs.acs.org/doi/10.1021/acsami.0c06211.

Additional experimental details, $J-V$ curves, top-view and cross-sectional SEM images, roughness of the film, contact angle test, XRD, SCLC measurement, PL and TRPL spectra, stability test, and EIS measurement (PDF)

AUTHOR INFORMATION

Corresponding Authors

Yu-Ching Huang − *Department of Materials Engineering, Ming Chi University of Technology, New Taipei City 24301, Taiwan;* orcid.org/0000-0003-4772-8050; Email: huangyc@mail.mcut.edu.tw

Wei-Fang Su − *Department of Materials Science and Engineering, National Taiwan University, Taipei 10617, Taiwan;* orcid.org/0000-0002-3375-4664; Email: suwf@ntu.edu.tw

Authors

Shih-Han Huang − *Department of Materials Science and Engineering, National Taiwan University, Taipei 10617, Taiwan*

Kuo-Yu Tian − *Department of Materials Science and Engineering, National Taiwan University, Taipei 10617, Taiwan*

Hung-Che Huang − *Department of Materials Science and Engineering, National Taiwan University, Taipei 10617, Taiwan*

Chia-Feng Li − *Department of Materials Engineering, Ming Chi University of Technology, New Taipei City 24301, Taiwan*

Wei-Cheng Chu − *Department of Chemical and Materials Engineering, Chang Gung University, Taoyuan 33302, Taiwan*

Kun-Mu Lee − *Department of Chemical and Materials Engineering, Chang Gung University, Taoyuan 33302, Taiwan; Division of Neonatology, Department of Pediatrics, Chang Gung Memorial Hospital, Taoyuan 33305, Taiwan;* orcid.org/0000-0002-5911-9386

Complete contact information is available at: https://pubs.acs.org/10.1021/acsami.0c06211

Author Contributions

The manuscript was written through the contribution of all authors.

Notes

The authors declare no competing financial interest.

ACKNOWLEDGMENTS

Financial support obtained from the Ministry of Science and Technology of Taiwan (MOST 108-3116-F-002-002-CC2 and MOST 107-2218-E-131-007-MY3), Academia Sinica (AS-SS-109-55), and Chang Gung Memorial Hospital, Linkou (CMRPD2G0302) is highly appreciated.

REFERENCES

(1) Snaith, H. J. Perovskites: The Emergence of a New Era for Low-Cost, High-Efficiency Solar Cells. *J. Phys. Chem. Lett.* **2013**, *4*, 3623−3630.

(2) Park, N.-G. Organometal Perovskite Light Absorbers Toward a 20% Efficiency Low-Cost Solid-State Mesoscopic Solar Cell. *J. Phys. Chem. Lett.* **2013**, *4*, 2423−2429.

(3) Kojima, A.; Teshima, K.; Shirai, Y.; Miyasaka, T. Organometal Halide Perovskites as Visible-Light Sensitizers for Photovoltaic Cells. *J. Am. Chem. Soc.* **2009**, *131*, 6050−6051.

(4) Chen, Q.; De Marco, N.; Yang, Y.; Song, T.-B.; Chen, C.-C.; Zhao, H.; Hong, Z.; Zhou, H.; Yang, Y. under the Spotlight: the Organic−Inorganic Hybrid Halide Perovskite for Optoelectronic Applications. *Nano Today* **2015**, *10*, 355−396.

(5) Dong, Q.; Fang, Y.; Shao, Y.; Mulligan, P.; Qiu, J.; Cao, L.; Huang, J. Electron-Hole Diffusion Lengths> 175 μm in Solution-Grown CH3NH3PbI3 Single Crystals. *Science* **2015**, *347*, 967−970.
(6) Zhang, Y.; Kim, S.-G.; Lee, D.; Shin, H.; Park, N.-G. Bifacial Stamping for High Efficiency Perovskite Solar Cells. *Energy Environ. Sci.* **2019**, *12*, 308−321.
(7) Lee, K.-M.; Lin, C.-J.; Liou, B.-Y.; Yu, S.-M.; Hsu, C.-C.; Suryanarayanan, V. Effect of Anti-Solvent Mixture on the Performance of Perovskite Solar Cells and Suppression Hysteresis Behavior. *Org. Electron.* **2019**, *65*, 266−274.
(8) Liao, H.-C.; Guo, P.; Hsu, C.-P.; Lin, M.; Wang, B.; Zeng, L.; Huang, W.; Soe, C. M. M.; Su, W.-F.; Bedzyk, M. J.; Wasielewski, M. R.; Facchetti, A.; Chang, R. P. H.; Kanatzidis, M. G.; Marks, T. J. Enhanced Efficiency of Hot-Cast Large-Area Planar Perovskite Solar Cells/Modules Having Controlled Chloride Incorporation. *Adv. Energy Mater.* **2017**, *7*, No. 1601660.
(9) Lee, P.-H.; Li, B.-T.; Lee, C.-F.; Huang, Z.-H.; Huang, Y.-C.; Su, W.-F. High-Efficiency Perovskite Solar Cell Using Cobalt Doped Nickel Oxide Hole Transport Layer Fabricated by NIR Process. *Sol. Energy Mater. Sol. Cells* **2020**, *208*, No. 110352.
(10) Wei, Z.; Chen, H.; Yan, K.; Yang, S. Inkjet Printing and Instant Chemical Transformation of a CH3NH3PbI3/Nanocarbon Electrode and Interface for Planar Perovskite Solar Cells. *Angew. Chem., Int. Ed.* **2014**, *53*, 13239−13243.
(11) Gheno, A.; Huang, Y.; Bouclé, J.; Ratier, B.; Rolland, A.; Even, J.; Vedraine, S. Toward Highly Efficient Inkjet-Printed Perovskite Solar Cells Fully Processed Under Ambient Conditions and at Low Temperature. *Solar RRL* **2018**, *2*, No. 1800191.
(12) Ramesh, M.; Boopathi, K. M.; Huang, T.-Y.; Huang, Y.-C.; Tsao, C.-S.; Chu, C.-W. Using an Airbrush Pen for Layer-by-Layer Growth of Continuous Perovskite Thin Films for Hybrid Solar Cells. *ACS Appl. Mater. Interfaces* **2015**, *7*, 2359−2366.
(13) Das, S.; Yang, B.; Gu, G.; Joshi, P. C.; Ivanov, I. N.; Rouleau, C. M.; Aytug, T.; Geohegan, D. B.; Xiao, K. High-Performance Flexible Perovskite Solar Cells by Using a Combination of Ultrasonic Spray-Coating and Low Thermal Budget Photonic Curing. *ACS Photonics* **2015**, *2*, 680−686.
(14) Mohamad, D. K.; Griffin, J.; Bracher, C.; Barrows, A. T.; Lidzey, D. G. Spray-Cast Multilayer Organometal Perovskite Solar Cells Fabricated in Air. *Adv. Energy Mater.* **2016**, *6*, No. 1600994.
(15) Bishop, J. E.; Smith, J. A.; Greenland, C.; Kumar, V.; Vaenas, N.; Game, O. S.; Routledge, T. J.; Wong-Stringer, M.; Rodenburg, C.; Lidzey, D. G. High-Efficiency Spray-Coated Perovskite Solar Cells Utilizing Vacuum-Assisted Solution Processing. *ACS Appl. Mater. Interfaces* **2018**, *10*, 39428−39434.
(16) Cui, X.-P.; Jiang, K.-J.; Huang, J.-H.; Zhou, X.-Q.; Su, M.-J.; Li, S.-G.; Zhang, Q.-Q.; Yang, L.-M.; Song, Y.-L. Electrodeposition of PbO and its in Situ Conversion to CH3NH3PbI3 for Mesoscopic Perovskite Solar Cells. *Chem. Commun.* **2015**, *51*, 1457−1460.
(17) Huang, J.-H.; Jiang, K.-J.; Cui, X.-P.; Zhang, Q.-Q.; Gao, M.; Su, M.-J.; Yang, L.-M.; Song, Y. Direct Conversion of CH3NH3PbI3 from Electrodeposited PbO for Highly Efficient Planar Perovskite Solar Cells. *Sci. Rep.* **2015**, *5*, No. 15889.
(18) Chen, H.; Wei, Z.; Zheng, X.; Yang, S. A Scalable Electrodeposition Route to the Low-Cost, Versatile and Controllable Fabrication of Perovskite Solar Cells. *Nano Energy* **2015**, *15*, 216−226.
(19) Jung, Y.-S.; Hwang, K.; Heo, Y.-J.; Kim, J.-E.; Lee, D.; Lee, C.-H.; Joh, H.-I.; Yeo, J.-S.; Kim, D.-Y. One-Step Printable Perovskite Films Fabricated under Ambient Conditions for Efficient and Reproducible Solar Cells. *ACS Appl. Mater. Interfaces* **2017**, *9*, 27832−27838.
(20) Di Giacomo, F.; Shanmugam, S.; Fledderus, H.; Bruijnaers, B. J.; Verhees, W. J. H.; Dorenkamper, M. S.; Veenstra, S. C.; Qiu, W.; Gehlhaar, R.; Merckx, T.; Aernouts, T.; Andriessen, R.; Galagan, Y. Up-Scalable Sheet-to-Sheet Production of High Efficiency Perovskite Module and Solar Cells on 6-in. Substrate Using Slot Die Coating. *Sol. Energy Mater. Sol. Cells* **2018**, *181*, 53−59.
(21) Lee, D.; Jung, Y.-S.; Heo, Y.-J.; Lee, S.; Hwang, K.; Jeon, Y.-J.; Kim, J.-E.; Park, J.; Jung, G. Y.; Kim, D.-Y. Slot-Die Coated Perovskite Films Using Mixed Lead Precursors for Highly Reproducible and Large-Area Solar Cells. *ACS Appl. Mater. Interfaces* **2018**, *10*, 16133−16139.
(22) Galagan, Y.; Di Giacomo, F.; Gorter, H.; Kirchner, G.; de Vries, I.; Andriessen, R.; Groen, P. Roll-to-Roll Slot Die Coated Perovskite for Efficient Flexible Solar Cells. *Adv. Energy Mater.* **2018**, *8*, No. 1801935.
(23) Huang, Y.-C.; Li, C.-F.; Huang, Z.-H.; Liu, P.-H.; Tsao, C.-S. Rapid and Sheet-to-Sheet Slot-Die Coating Manufacture of Highly Efficient Perovskite Solar Cells Processed under Ambient Air. *Solar Energy* **2019**, *177*, 255−261.
(24) Deng, Y.; Peng, E.; Shao, Y.; Xiao, Z.; Dong, Q.; Huang, J. Scalable Fabrication of Efficient Organolead Trihalide Perovskite Solar Cells with Doctor-Bladed Active Layers. *Energy Environ. Sci.* **2015**, *8*, 1544−1550.
(25) Tang, S.; Deng, Y.; Zheng, X.; Bai, Y.; Fang, Y.; Dong, Q.; Wei, H.; Huang, J. Composition Engineering in Doctor-Blading of Perovskite Solar Cells. *Adv. Energy Mater.* **2017**, *7*, No. 1700302.
(26) Wu, W.-Q.; Wang, Q.; Fang, Y.; Shao, Y.; Tang, S.; Deng, Y.; Lu, H.; Liu, Y.; Li, T.; Yang, Z.; Gruverman, A.; Huang, J. Molecular Doping Enabled Scalable Blading of Efficient Hole-Transport-Layer-Free Perovskite Solar Cells. *Nat. Commun.* **2018**, *9*, No. 1625.
(27) Zhong, Y.; Munir, R.; Li, J.; Tang, M.-C.; Niazi, M. R.; Smilgies, D.-M.; Zhao, K.; Amassian, A. Blade-Coated Hybrid Perovskite Solar Cells with Efficiency> 17%: An in Situ Investigation. *ACS Energy Lett.* **2018**, 1078−1085.
(28) Deng, Y.; Zheng, X.; Bai, Y.; Wang, Q.; Zhao, J.; Huang, J. Surfactant-Controlled Ink Drying Enables High-Speed Deposition of Perovskite Films for Efficient Photovoltaic Modules. *Nat. Energy* **2018**, *3*, 560−566.
(29) Bi, Z.; Rodríguez-Martínez, X.; Aranda, C.; Pascual-San-José, E.; Goñi, A. R.; Campoy-Quiles, M.; Xu, X.; Guerrero, A. Defect Tolerant Perovskite Solar Cells from Blade Coated Non-Toxic Solvents. *J. Mater. Chem. A* **2018**, *6*, 19085−19093.
(30) Wu, W.-Q.; Yang, Z.; Rudd, P. N.; Shao, Y.; Dai, X.; Wei, H.; Zhao, J.; Fang, Y.; Wang, Q.; Liu, Y.; Deng, Y.; Xiao, X.; Feng, Y.; Huang, J. Bilateral Alkylamine for Suppressing Charge Recombination and Improving Stability in Blade-Coated Perovskite Solar Cells. *Sci. Adv.* **2019**, *5*, No. eaav8925.
(31) van Reenen, S.; Kemerink, M.; Snaith, H. J. Modeling Anomalous Hysteresis in Perovskite Solar Cells. *J. Phys. Chem. Lett.* **2015**, *6*, 3808−3814.
(32) Kang, D.-H.; Park, N.-G. On the Current−Voltage Hysteresis in Perovskite Solar Cells: Dependence on Perovskite Composition and Methods to Remove Hysteresis. *Adv. Mater.* **2019**, *31*, No. 1805214.
(33) Liu, C.; Cai, M.; Yang, Y.; Arain, Z.; Ding, Y.; Shi, X.; Shi, P.; Ma, S.; Hayat, T.; Alsaedi, A.; Wu, J.; Dai, S.; Cao, G. A C60/TiOx Bilayer for Conformal Growth of Perovskite Films for UV Stable Perovskite Solar Cells. *J. Mater. Chem. A* **2019**, *7*, 11086−11094.
(34) Dong, H.; Yue, M.; Pang, S.; Zhu, W.; Chen, D.; Xi, H.; Lin, Z.; Chang, J.; Zhang, J.; Hao, Y.; Zhang, C. A Modulated Double-Passivation Strategy Toward Highly Efficient Perovskite Solar Cells with Efficiency Over 21%. *Solar RRL* **2019**, *3*, No. 1900291.
(35) Shi, D.; Qin, X.; Li, Y.; He, Y.; Zhong, C.; Pan, J.; Dong, H.; Xu, W.; Li, T.; Hu, W.; Brédas, J.-L.; Bakr, O. M. Spiro-OMeTAD Single Crystals: Remarkably Enhanced Charge-Carrier Transport via Mesoscale Ordering. *Sci. Adv.* **2016**, *2*, No. e1501491.
(36) Namatame, M.; Yabusaki, M.; Watanabe, T.; Ogomi, Y.; Hayase, S.; Marumoto, K. Direct Observation of Dramatically Enhanced Hole Formation in a Perovskite-Solar-Cell Material Spiro-OMeTAD by Li-TFSI Doping. *Appl. Phys. Lett.* **2017**, *110*, No. 123904.
(37) Lamberti, F.; Gatti, T.; Cescon, E.; Sorrentino, R.; Rizzo, A.; Menna, E.; Meneghesso, G.; Meneghetti, M.; Petrozza, A.; Franco, L. Evidence of Spiro-OMeTAD De-doping by tert-Butylpyridine

https://dx.doi.org/10.1021/acsami.0c06211
ACS Appl. Mater. Interfaces 2020, 12, 26041−26049

Additive in Hole-Transporting Layers for Perovskite Solar Cells. *Chem* **2019**, *5*, 1806−1817.
(38) Sun, K.; Wang, Y.; Xu, H.; Zhang, J.; Zhu, Y.; Hu, Z. Short-Term Stability of Perovskite Solar Cells Affected by in Situ Interface Modification. *Solar RRL* **2019**, *3*, No. 1900089.
(39) Huang, Y.-C.; Cha, H.-C.; Chen, C.-Y.; Tsao, C.-S. A Universal Roll-to-Roll Slot-Die Coating Approach Towards High-Efficiency Organic Photovoltaics. *Prog. Photovoltaics* **2017**, *25*, 928−935.
(40) Hansen, C. M. *The Three Dimensional Solubility Parameter*; Danish Technical Press: Copenhagen, 1967; p 14.
(41) Gutmann, V. Solvent Effects on the Reactivities of Organometallic Compounds. *Coord. Chem. Rev.* **1976**, *18*, 225−255.
(42) Cramer, R. E.; Bopp, T. T. Great E and C Plot. Graphical Display of the Enthalpies of Adduct Formation for Lewis Acids and Bases. *J. Chem. Educ.* **1977**, *54*, 612.
(43) Tait, J. G.; Merckx, T.; Li, W.; Wong, C.; Gehlhaar, R.; Cheyns, D.; Turbiez, M.; Heremans, P. Determination of Solvent Systems for Blade Coating Thin Film Photovoltaics. *Adv. Funct. Mater.* **2015**, *25*, 3393−3398.
(44) Gardner, K. L.; Tait, J. G.; Merckx, T.; Qiu, W.; Paetzold, U. W.; Kootstra, L.; Jaysankar, M.; Gehlhaar, R.; Cheyns, D.; Heremans, P.; Poortmans, J. Nonhazardous Solvent Systems for Processing Perovskite Photovoltaics. *Adv. Energy Mater.* **2016**, *6*, No. 1600386.
(45) Wang, J.; Di Giacomo, F.; Brüls, J.; Gorter, H.; Katsouras, I.; Groen, P.; Janssen, R. A. J.; Andriessen, R.; Galagan, Y. Highly Efficient Perovskite Solar Cells Using Non-Toxic Industry Compatible Solvent System. *Solar RRL* **2017**, *1*, No. 1700091.
(46) Chen, H.; Ye, F.; Tang, W.; He, J.; Yin, M.; Wang, Y.; Xie, F.; Bi, E.; Yang, X.; Grätzel, M.; Han, L. A Solvent- and Vacuum-Free Route to Large-Area Perovskite Films for Efficient Solar Modules. *Nature* **2017**, *550*, 92−95.
(47) Stoumpos, C. C.; Malliakas, C. D.; Kanatzidis, M. G. Semiconducting Tin and Lead Iodide Perovskites with Organic Cations: Phase Transitions, High Mobilities, and Near-Infrared Photoluminescent Properties. *Inorg. Chem.* **2013**, *52*, 9019−9038.
(48) Foley, B. J.; Girard, J.; Sorenson, B. A.; Chen, A. Z.; Scott Niezgoda, J.; Alpert, M. R.; Harper, A. F.; Smilgies, D.-M.; Clancy, P.; Saidi, W. A.; Choi, J. J. Controlling Nucleation, Growth, and Orientation of Metal Halide Perovskite Thin Films with Rationally Selected Additives. *J. Mater. Chem. A* **2017**, *5*, 113−123.
(49) Cho, N.; Li, F.; Turedi, B.; Sinatra, L.; Sarmah, S. P.; Parida, M. R.; Saidaminov, M. I.; Murali, B.; Burlakov, V. M.; Goriely, A.; Mohammed, O. F.; Wu, T.; Bakr, O. M. Pure Crystal Orientation and Anisotropic Charge Transport in Large-Area Hybrid Perovskite Films. *Nat. Commun.* **2016**, *7*, No. 13407.
(50) Chang, C.-Y.; Chu, C.-Y.; Huang, Y.-C.; Huang, C.-W.; Chang, S.-Y.; Chen, C.-A.; Chao, C.-Y.; Su, W.-F. Tuning Perovskite Morphology by Polymer Additive for High Efficiency Solar Cell. *ACS Appl. Mater. Interfaces* **2015**, *7*, 4955−4961.
(51) Chang, C.-Y.; Huang, Y.-C.; Tsao, C.-S.; Su, W.-F. Formation Mechanism and Control of Perovskite Films from Solution to Crystalline Phase Studied by in Situ Synchrotron Scattering. *ACS Appl. Mater. Interfaces* **2016**, *8*, 26712−26721.
(52) Chang, C.-Y.; Wang, C.-P.; Raja, R.; Wang, L.; Tsao, C.-S.; Su, W.-F. High-Efficiency Bulk Heterojunction Perovskite Solar Cell Fabricated by One-Step Solution Process Using Single Solvent: Synthesis and Characterization of Material and Film Formation Mechanism. *J. Mater. Chem. A* **2018**, *6*, 4179−4188.
(53) Tan, H.; Jain, A.; Voznyy, O.; Lan, X.; García de Arquer, F. P.; Fan, J. Z.; Quintero-Bermudez, R.; Yuan, M.; Zhang, B.; Zhao, Y.; Fan, F.; Li, P.; Quan, L. N.; Zhao, Y.; Lu, Z.-H.; Yang, Z.; Hoogland, S.; Sargent, E. H. Efficient and Stable Solution-Processed Planar Perovskite Solar Cells via Contact Passivation. *Science* **2017**, *355*, 722−726.
(54) Courtier, N. E.; Cave, J. M.; Foster, J. M.; Walker, A. B.; Richardson, G. How Transport Layer Properties Affect Perovskite Solar Cell Performance: Insights from a Coupled Charge Transport/Ion Migration Model. *Energy Environ. Sci.* **2019**, *12*, 396−409.

https://dx.doi.org/10.1021/acsami.0c06211
ACS Appl. Mater. Interfaces 2020, 12, 26041−26049